Journal of CO2 Utilization 105 (2026) 103357

Contents lists available at ScienceDirect

Journal of CO2 Utilization

journal homepage: www.elsevier.com/locate/jcou

Revealing the structure-activity relationship of Mn_3O_4/TiO_2 via phase engineering for enhanced photocatalytic CO_2 reduction

Eunhee Gong [a], Hye Rim Kim [a], Yunju Hwang [a], Jeonghyeon Lee [a], Jin-Woo Jung [b], Chang-Hee Cho [b], In Young Kim [c,*], Su-Il In [a,*]

[a] Department of Energy Science & Engineering, Daegu Gyeongbuk Institute of Science & Technology (DGIST), 333 Techno Jungang-daero, Hyeonpung-eup, Dalseong-gun, Daegu 42988, Republic of Korea
[b] Department of Physics and Chemistry, Daegu Gyeongbuk Institute of Science & Technology (DGIST), 333 Techno Jungang-daero, Hyeonpung-eup, Dalseong-gun, Daegu 42988, Republic of Korea
[c] Department of Chemistry and Nanoscience, College of Natural Science, Ewha Womans University, Seoul 03760, Republic of Korea

ARTICLE INFO

Keywords:
Phase engineering
Oxidation states
Reaction intermediates
CO_2 reduction
Photocatalysis

ABSTRACT

The structure-activity relationship plays a crucial role for enhanced photocatalytic performance, nevertheless, precisely controlling the phase of transition metal oxides remains a significant challenge. Herein, we developed 2D-layered Mn_3O_4 decorated with TiO_2 catalyst to investigate the effects of manganese oxide phase on photocatalytic CO_2 reduction activity. We optimized the manganese oxide phase by varying the amount of the $TiCl_4$ precursor. During the synthesis reaction, $TiCl_4$ is a key role for determining the oxidation state of manganese oxide. We identified that Mn_3O_4 is the best phase for photocatalytic CO_2 reduction, and Mn_3O_4/TiO_2 exhibits 20.1-, 7.8-fold enhanced photocatalytic CO_2 reduction performance than pristine TiO_2 and Mn_3O_4, respectively. The improved photocatalytic activity is relevant to the phase of manganese oxide, the enhanced separation of charge carriers and prolonged lifetimes of charge carriers. *In situ* X-ray Absorption Near-Edge Structure (XANES) confirms the changes of oxidation state under photocatalytic CO_2 reduction conditions. Furthermore, the photocatalytic mechanism is proposed by *in situ* Diffuse Reflectance Infrared Fourier Transform Spectroscopy (DRIFTS) analysis. This study provides an effective design strategy for modulating oxidation state of transition metal oxide-based photocatalyst for enhanced solar fuels generation.

1. Introduction

Photocatalytic CO_2 reduction into hydrocarbon fuels offers an appealing solution to both energy and environmental problems with solar energy stored in the form of chemical energy compatible with the current energy infrastructure [1–3]. To date, various semiconductor-based photocatalysts such as TiO_2[4,5], ZnO [6,7], and CdS [8–10], have been studied for their application in photocatalytic CO_2 reduction. Among the materials studied, TiO_2 has proven to be of most interest owing to its non-toxicity, chemical stability, and low cost [11,12]. However, TiO_2 has a relatively large band gap that in turn limits its response to the UV region [13,14] and shows fast recombination. Numerous efforts have been reported to improve upon TiO_2, including the use of co-catalysts [15,16], facet engineering [17,18], the help of sacrificial agents or photosensitizers [19,20], and the formation of heterostructured catalysts [21,22].

Manganese oxides have been widely studied within the supercapacitor field due to their high capacitance and superb stability [23,24]. Recently, manganese oxide-based materials have been considered as promising photocatalyst [25,26] due to their visible-spectrum light absorption, excellent chemical stability, and environmental compatibility [27]. However, further research on the utility of manganese oxide-based materials for photocatalytic CO_2 reduction is needed.

Recent studies reported that the oxidation state of a transition metal plays an important role in determining catalytic activity [28]. Since a transition metal has d-orbital electrons, it can have variable oxidation states. Rajeshwar *et al.* studied the correlation between the oxidation state of Cu over copper oxide-based materials and photoelectrocatalytic CO_2 conversion efficiency [29]. It is noted that mixed-phase compositions with different oxidation states result in low CO_2 reduction efficiency, with the photogenerated electrons unable to overcome the activation energy barrier required for CO_2 reduction. Therefore,

* Corresponding authors.
E-mail addresses: iykim@ewha.ac.kr (I.Y. Kim), insuil@dgist.ac.kr (S.-I. In).

https://doi.org/10.1016/j.jcou.2026.103357
Received 10 November 2025; Received in revised form 4 February 2026; Accepted 8 February 2026
Available online 16 February 2026
2212-9820/© 2026 The Authors. Published by Elsevier Ltd. This is an open access article under the CC BY license (http://creativecommons.org/licenses/by/4.0/).

controlling the oxidation state of a transition metal element is a promising approach for improving photocatalytic CO_2 reduction efficiency.

To date, the majority of reported photocatalytic reactions have been evaluated using high concentrations of CO_2 (99 %), which is far higher than actual concentration of CO_2 in atmosphere (~ 400 ppm). Recently, Liao's group reported photocatalytic reduction of low concentration CO_2 (10 %) into syngas by graphene-modified transition metal hydroxides [30]. Still, achieving high selectivity for hydrocarbons remains a significant challenge for the low concentration of CO_2 environment.

Herein, we successfully fabricated a novel Mn_3O_4/TiO_2 photocatalyst by precisely engineering the phase of the manganese oxide, which resulted in an ideal oxidation state of manganese oxide and improved CO_2 photoreduction. This strategic design resulted in an ideal oxidation state that enables the efficient and selective production of CH_4 under 1000 ppm CO_2. The phase of manganese oxide was identified by X-ray diffraction, and the oxidation state of manganese was confirmed using X-ray photoelectron spectroscopy (XPS). The results show that the amount of $TiCl_4$ precursors determines manganese oxide phase, and the oxidation state of manganese plays a crucial role in photocatalytic activity. Based on the *in situ* XANES and *in situ* DRIFTS analysis, the effect of the valence state and the photocatalytic mechanism, respectively, are proposed and discussed in depth. Our work can provide an insight for the strategy of controlling the oxidation state to improve the photocatalytic performance, which can be applicable for solar fuels generation.

2. Experimental

2.1. Materials

Sodium dodecyl sulfate (SDS, Sigma Aldrich, 99.0 %), potassium permanganate ($KMnO_4$, Sigma Aldrich, 99.0 %), concentrated sulfuric acid (0.1 M H_2SO_4 in water, Sigma Aldrich),and titanium(IV) chloride ($TiCl_4$, Sigma Aldrich, 99.9 %).

2.2. Synthesis of MnO_2 nanosheets

MnO_2 nanosheets were synthesized by the previously reported method [31]. Briefly, 98 mL of SDS solution (0.1 M) and 4.8 mL of H_2SO_4 solution (0.1 M) were added into 283.2 mL of deionized water and then heated at 95 °C. After reaching 95 °C, 3.6 mL of $KMnO_4$ solution (0.4 M) was mixed with the solution and heated for 1 h at 95 °C. The resulting brown colored solution was cooled at room temperature, and washed several times with deionized water and ethanol, followed by freeze-drying for 2 days to obtain MnO_2 nanosheets.

2.3. Synthesis of Mn_3O_4/TiO_2 photocatalyst

A 200 mg sample of MnO_2 nanosheets was dispersed in 6 mL of anhydrous toluene in a rubber-capped vial and degassed with vacuum and Ar. $TiCl_4$ with a different molar ratio of Ti/Mn was added to the solution while stirring. The solution was further stirred in air for 30 min so that the $TiCl_4$ reduces MnO_2 and changes to TiO_2. The mixture was dried before being calcined in air at 400 °C for 1 h. The samples with different molar ratios of $TiCl_4$ were denoted as MTx, where x = 0.8, 0.9, 1.0, 1.1, and 1.2 represent the molar ratio of Ti when Mn is fixed at 1.

2.4. Synthesis of pristine Mn_3O_4 photocatalyst

To synthesize pristine Mn_3O_4 as a control sample, MnO_2 nanosheets were reacted with HCl instead of $TiCl_4$. The amount of added HCl was adjusted to match the molar ratio (Mn:Ti = 1:1), ensuring a consistent reducing environment. The resulting product was washed and calcined under the same conditions as the MTx samples.

2.5. Characterization of photocatalysts

Sample crystallinity was determined by X-ray diffractometer (XRD, Rigaku, MiniFlex600) operated at 40 kV and 30 mA with Cu Kα radiation (λ=1.54 Å). The surface morphologies were characterized by a field emission scanning electron microscope (FE-SEM, Hitachi, S-4800) with an accelerating voltage of 3 kV; elemental mapping was measured using energy dispersive spectroscopy (EDS). High resolution images were obtained by a field emission transmission electron microscope (FE-TEM, Hitachi, HF-3300) operating at 300 kV. XPS (Thermo Scientific, ESCALAB 250Xi) and valence band-XPS (VB-XPS) were performed using Al Kα line (1486.6 eV) as the X-ray source. XANES and *in-situ* X ANES spectra were collected by the BL10C beamline at the Pohang Light Source (PLS-II). UV-Visible diffuse reflectance spectra (UV-Vis DRS) of samples were recorded by a UV-Visible near infrared spectrophotometer (Agilent, Cary 5000) with a diffuse reflection accessory. Photoluminescence (PL) spectra were measured using a fluorescence spectrophotometer (Agilent, Cary Eclipse) with a 300 nm excitation wavelength. The time-resolved PL (TRPL) measurements were performed by using a home-built confocal micro-PL setup. Samples were excited by a pico-second pulsed diode laser (PicoQuant, LDH-P-C-450B) with the wavelength of 454 nm (FWHM ≈ 60 ps) and a repetition rate of 40 MHz. The laser beam was focused by a 40x (NA=0.6) objective (Nikon). The PL decay signal was detected by a hybrid photomultiplier detector (PicoQuant, PMA hybrid series) and a time-correlated single photon counting system (PicoQuant).

2.6. Photocatalytic CO_2 reduction test

CO_2 photoreduction experiments were conducted in a customized batch reactor system at a controlled temperature of 22 °C ± 2 °C. 50 mg of photocatalyst was loaded into a stainless-steel reactor (volume=15.4 cm^3) with a quartz window. Prior to illumination, the reactor was first vacuum purged, then CO_2 (1000 ppm in He) passing through a water bubbler, was flowed through the chamber for 1 h. A 100 W Xe lamp (Oriel, LCS-100) with an AM 1.5 filter was used as a light source. The reactor was illuminated for 1 h, after which a 500 μL gaseous sample was taken and injected into a gas chromatograph unit (Shimadzu, GC-2014) equipped with a flame ionization detector (FID, Restek Rt-Q-bond column, ID = 0.53 mm, length = 30 m). Each sample was tested three times under the same experimental conditions; the CH_4 evolution rate shown is the average value. The hydrocarbon product yield was calculated by following equation.

$$\text{Total hydrocarbon yield}\left(\mu\text{mol} \bullet g^{-1} \bullet h^{-1}\right) = \frac{\left(C_{final} - C_{initial}\right) \times \text{volume}}{\text{Amount of photocatalyst used}(g) \times \text{time}(h)}$$

A stability test was carried out using best performed sample MT1.0, cycling it through five cycles of CO_2 photoreduction experiments. After every cycle, to regenerate the catalyst, the catalyst was vacuum annealed at 100 °C for 2 h and the reactor was purged, as before, with vacuum and CO_2 gas (1000 ppm in He).

Control and isotopic tests were performed to confirm CO_2 as the origin of carbon source. A control test was carried out using an He/H_2O (g) mixture instead of moist CO_2 under the same experimental conditions. An isotopic test was conducted by $^{13}CO_2$ gas (99 %, Sigma Aldrich) diluted to a concentration of 1000 ppm in pure He gas (99.999 %). The obtained products were analyzed by use of a gas chromatography-mass spectrometer (Shimadzu, GC-MS-QP2010 Ultra, Restek Rt-Q-Bond column, ID = 0.32 mm, length = 30 m).

2.7. Examination of photocatalytic CO_2 reduction mechanism

To disclose the photocatalytic CO_2 reduction mechanism, *in situ* DRIFTS spectra were obtained using nicolet is50 spectrometer (Thermo

Fisher Scientific) equipped with an HgCdTe (MCT) detector. The spectra were acquired with a resolution of 4 cm^{-1} using 32 scans. *In situ* DRIFTS reaction chamber (Harrick Scientific) with two ZnSe and one quartz window was used to perform the experiment. Prior to test, the sample was heated to 100 °C in a vacuum for 2 h to remove the adsorbed molecules. After cooling down the chamber to room temperature, CO_2 (1000 ppm in He) and H_2O vapor were flowed into the chamber and maintained for 30 min. Then, the light was illuminated through quartz window for 60 min. Xe lamp (300 W, AM 1.5 filter) with focusing fiber was used as a light source and the data was collected every 15 min.

3. Results and discussion

3.1. Structure analysis and morphology properties

XRD spectra (Fig. S1) shows that all the samples are comprised of Mn_3O_4 and anatase TiO_2, confirming the formation of $Mn3O_4/TiO_2$ composite. The XRD peaks at 2θ values of 18.0°, 28.8°, 32.3°, and 36.1° respectively correspond to (1 0 1), (1 1 2), (1 0 3), and (2 1 1) planes, indicating the presence of Mn_3O_4, spinel hausmannite structure (ICDD 00–024–0737). XRD patterns at 2θ values of 25.3°, 37.5°, and 47.9° are consistent with (1 0 1), (0 0 4), and (2 0 0) planes, respectively, implying the presence of anatase TiO_2 (ICDD 01–071–1168). Notably, the final manganese oxide phase of the MTx exhibited differences depending on the concentration of $TiCl_4$ precursor. During synthesizing MTx sample, $TiCl_4$ reacts with water and produce HCl. The generated HCl determines the degree of reduction of the initial MnO_2, which leads to differences in the composition of final product. In the case of the samples with low content of Ti, as seen for MT0.8 and MT0.9 samples, hydrolysis of $TiCl_4$ was limited, resulting in insufficient production of HCl. Consequently, MnO_2 was incompletely reduced, producing MnOOH. In contrast, MT1.0, MT1.1 and MT1.2 samples, which had high Ti contents, a large amount of HCl was produced, creating a strongly reducing environment. Under these conditions, MnO_2 completely reduced to the Mn_3O_4 phase without forming MnOOH intermediate. Also, $MnCl_2$ byproduct were detected in all samples with its XRD peaks increasing with a higher $TiCl_4$ content. For comparison, pristine Mn_3O_4 was synthesized by reduction of MnO_2 using HCl, and its structural and morphological properties are presented in Fig. S2.

The surface morphology of MnO_2 and MT1.0 samples were acquired by FE-SEM and FE-TEM analysis. MnO_2 has a two-dimensional (2D)-layered structure (Fig. S3), and MT1.0 maintains the 2D-layered

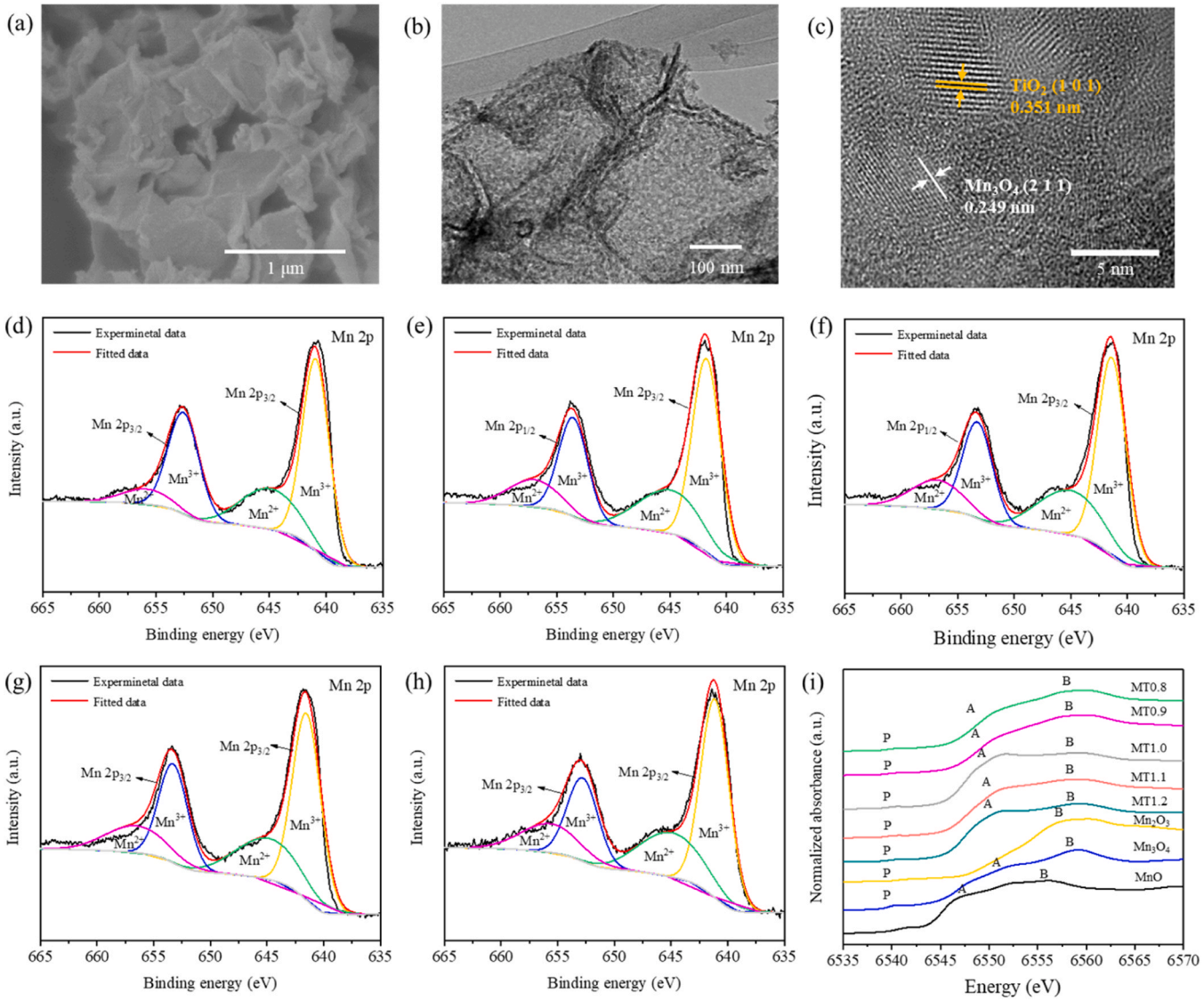


Fig. 1. (a) SEM images, (b) TEM images, and (c) HR-TEM images of MT1.0. HR-XPS spectra for Mn 2p peak of (d) MT0.8, (e) MT0.9, (f) MT1.0, (g) MT1.1, and (h) MT1.2. (i) Mn K-edge XANES spectra of MT0.8–1.2 samples, Mn_2O_3, Mn_3O_4 and MnO.

structure even after annealing at 400 °C (Fig. 1a). Low- and high- resolution TEM images show that the 2D-layered structure in sample MT1.0 possesses a d-spacing of 0.351 nm for the TiO_2 (1 0 1) plane [32], and 0.249 nm for the Mn_3O_4 (2 1 1) plane [33], in agreement with the XRD results (Fig. 1b, c). EDS mapping and spectrum confirm that MT1.0 shows the well distributed Mn, Ti, and O elements (Fig S4), demonstrating MT1.0 has an intimate Mn_3O_4/TiO_2 configuration.

Sample chemical states were affirmed by XPS investigation, and all peaks were fitted using the Shirley-type background method [34]. Fig. 1d-h show the high resolution XPS (HR-XPS) spectra of Mn 2p for MT0.8–1.2 samples, respectively. The Mn $2p_{1/2}$ and $2p_{3/2}$ peaks were deconvoluted into two peaks by Mn^{2+} and Mn^{3+}, which are associated with the peak positions at 655.5–656.8 eV (Mn^{2+} $2p_{1/2}$), 652.6–653.5 eV (Mn^{3+} $2p_{1/2}$), 644.8–645.0 eV (Mn^{2+} $2p_{3/2}$), and 640.9–641.7 eV (Mn^{3+} $2p_{3/2}$), respectively. The results indicate that the Mn atoms have a mixed valence state of Mn^{3+}/Mn^{2+} in each MTx sample [35]. The ratio of Mn $2p_{1/2}$ peak area (Mn^{3+}/Mn^{2+}) for MT0.8 is 4.30, MT0.9 is 2.11, MT1.0 is 1.95, MT1.1 is 1.75, and MT1.2 is 1.54 (Table S1). The calculated oxidation state of Mn atoms in MTx is + 2.811, + 2.679, + 2.661, + 2.636, + 2.545 for MT0.8, MT0.9, MT1.0, MT1.1 and MT1.2, respectively. Among them, sample MT1.0 has the nearest value to the oxidation state of Mn atoms for Mn_3O_4 of + 2.667 [36]. The oxidation state of the Mn atoms and local atomic structure of MTx sample were further confirmed by the Mn K-edge XANES analysis (Fig. 2i). Every absorption edge energy of MTx sample displays between the one of MnO and Mn_2O_3, indicating that the Mn ions in MT0.8–1.2 samples show mixed valence states of + 2 and + 3. Overall spectral features of MT0.8–1.2 samples are very similar to those of Mn_3O_4, indicating that they exhibit the crystal structure of Mn_3O_4. The Mn_3O_4 has spinel structure, in which the Mn^{2+} occupy the T_d sites whereas the Mn^{3+} occupy the O_h sites. The weak pre-edge peak, P for all present samples corresponds to partially allowed Mn 1 s → Mn 3d transition, which appears due to Jahn-Teller distortion of Mn^{3+} in O_h sites [37]. The main feature of A is referred as the ligand to metal charge transfer (O 2p → Mn 3d) while the main feature B is attributed to Mn 1 s → Mn 4p transition [34]. The feature A is more distinct for MT1.0, MT1.1, and MT1.2 rather than MT0.8, MT0.9, and Mn_3O_4. The intense ligand to metal charge transfer in MT1.0, MT1.1, and MT1.2 accompanies strong visible light absorption. In addition, HR-XPS spectra of O 1 s and Ti 2p for MT0.8–1.2 samples were obtained (Fig. S5). The O 1 s peak was resolved into three peaks at binding energies of 529.51 eV, 530.62 eV, and 531.82 eV, which can be attributed to the oxygen lattice in TiO_2 [38], lattice oxygen in Mn_3O_4 [39], and adsorbed oxygen molecules [40], respectively. The binding energy values of 464.01 and 458.19 eV with difference of 5.8 eV between the two peaks are matched with Ti $2p_{1/2}$ and Ti $2p_{3/2}$, originating from Ti^{4+} oxidation state [41].

3.2. Band structure analysis

To elucidate the electronic band structure, UV-Vis DRS and VB-XPS spectra were obtained. As shown in Fig. 2a, anatase TiO_2 exhibits absorption only in the UV range ($\lambda < 400$ nm) [42]. Compared to the TiO_2, MT0.8–1.2 samples clearly show the increased absorption in the visible region (400–800 nm) due to the visible-active Mn_3O_4. Furthermore, MT1.0–1.2 samples present more enhanced visible light absorption in the region of 400–550 nm. This fact cross-confirms the intense

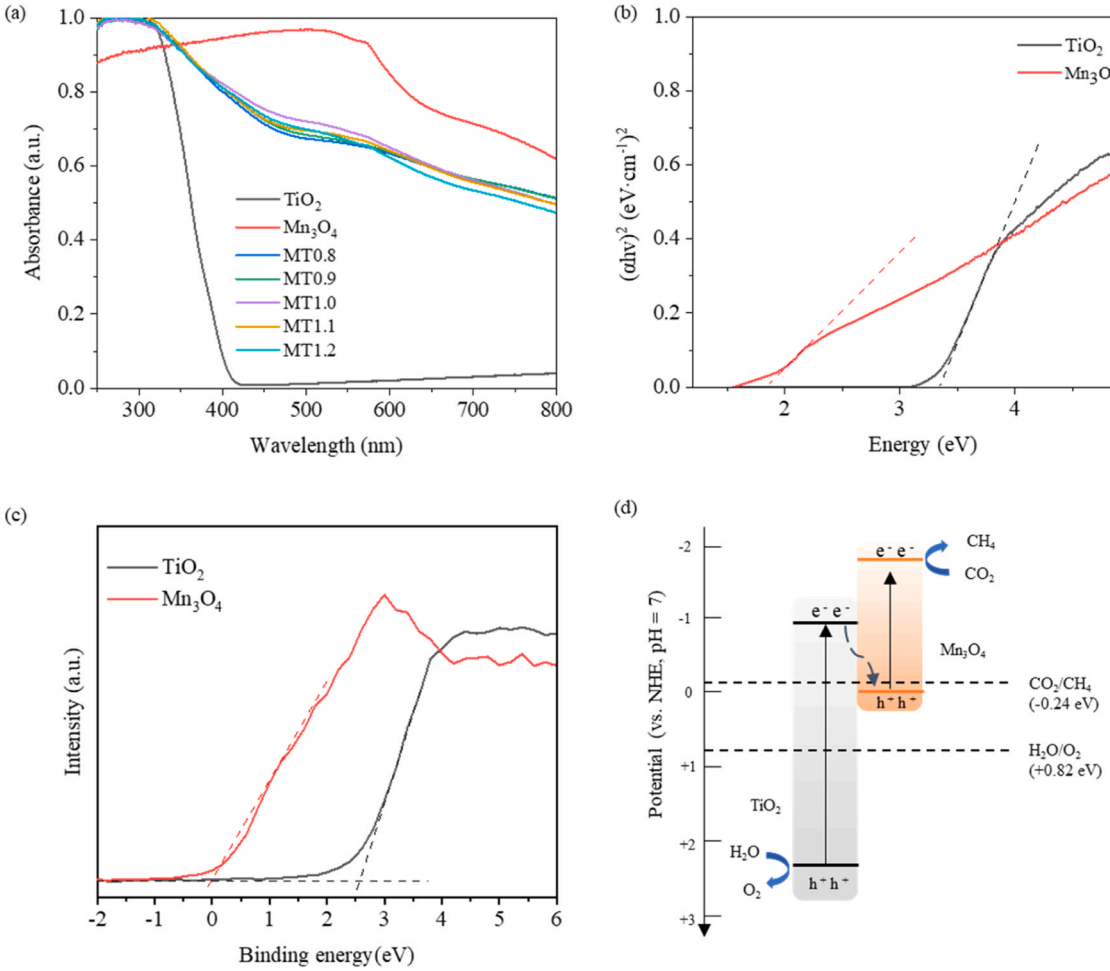


Fig. 2. (a) UV-Vis DRS spectra of TiO_2, Mn_3O_4, and MTx samples. (b) band gap, and (c) VB-XPS results for Mn_3O_4 and TiO_2. (d) Schematic band structure of MT1.0.

ligand-to-metal charge transfer in MT1.0–1.2 as proved in the XANES result. Band gaps were calculated by Tauc plot using corresponding UV-Vis DRS. Tauc plots were acquired by plotting $(\alpha h\nu)^n$ and $E_g = h\nu$ (where α is absorption coefficient, *h* is Planks constant, *ν* is frequency, n = 1/2 for direct band gap of Mn_3O_4 and TiO_2, and E_g is band gap) [43]. It is observed that Mn_3O_4 shows a band gap of 1.88 eV, a value in agreement with literature [44], and TiO_2 shows a band gap of 3.31 eV (Fig. 2b) [45]. Fig. 2c displays that the VB-XPS of Mn_3O_4 and TiO_2 were located at −0.01 eV and 2.55 eV, respectively. The position of conduction band (CB) can be calculated by using obtained band gap and VB-XPS results. The CB of Mn_3O_4 and TiO_2 are calculated to be – 1.89 eV and -0.70 eV, respectively. Based on the results, schematic band structure of MT1.0 is obtained, which is suitable for photocatalytic CO_2 reduction to CH_4 (Fig. 2d). MT1.0 forms a direct Z-scheme structure, which significantly enhances the redox potential of the system. Specifically, the photogenerated electrons in the CB of TiO_2 migrate to the VB of Mn_3O_4. This process allows the high energy electrons in the CB of Mn_3O_4 to be effectively perform CO_2 reduction to CH_4. Simultaneously, the holes remaining in the VB of TiO_2 are utilized for the oxidation of H_2O to O_2. This Z-scheme mechanism facilitates efficient spatial separation of carriers and maximizes the thermodynamic driving force for both oxidation and reduction reactions [46].

3.3. Charge separation and photocatalytic activity

To understand the dynamics of photogenerated charge carriers, PL and TRPL analysis were performed. The charge separation ability was evaluated by PL (Fig. S6). It has been reported that TiO_2 shows significant PL emission peak due to recombination of photogenerated electrons [47], which is vulnerable to photocatalytic performance. All MTx samples show significantly suppressed PL emission peak, which implies photogenerated electron-hole pairs were successfully separated, decreasing the recombination rate [48,49]. To gain further insight of charge carriers, TRPL decay spectra (Fig. S7) were performed, which were fitted with a bi-exponential function in the decay profiles [50]. More specifically, the following function was used to fit the TRPL decay profiles:

$$I(t) = A1 \bullet \exp(-\frac{t}{\tau 1}) + A2 \bullet \exp(-\frac{t}{\tau 2})$$

where I(t) is the intensity of the PL signal, τ_1 and τ_2 are the carrier lifetime, and A_1 and A_2 are the corresponding magnitudes. All parameters and average lifetime of charge (τ_{ave}) for MTx samples are listed in Table S2. Among the MTx samples, MT1.0 shows the longest charge carrier average lifetime (0.8084 ns). It is well known that material with longer lifetime of charge carrier has more chance to participate in photocatalytic reaction; therefore, it can show higher photocatalytic performance than that of shorter lifetime of charge carrier [51]. The photocatalytic performance is relevant to the lifetime of charge carriers, which is discussed below.

The CO_2 photoreduction activities of TiO_2, Mn_3O_4, and MTx samples were monitored in a gas-solid reaction setup in the presence of CO_2 and H_2O vapor under simulated solar irradiation (Fig. S8). Fig. 3a demonstrates the photocatalytic CH_4 production rates and charge carrier average lifetimes for the MTx samples. The MTx samples show an increased CH_4 evolution rate as the Ti fraction increased in the composite until the molar ratio of Ti component was 1.0. The highest average CH_4 yield was observed in sample MT1.0 (0.0902 $\mu mol \bullet g^{-1} \bullet h^{-1}$); the average CH_4 yield decreased as the molar ratio of Ti increased over 1.0 (Table S3). This trend is similar to that of charge carrier lifetimes, where sample MT1.0 shows the longest average lifetime, implying that the lifetime of charge carriers is highly correlated to photocatalytic performance. This correlation is further clarified by the phase impurities observed in the other samples. MT0.8 and MT0.9 samples exhibited lower activity due to the presence of a residual MnOOH phase mixed with Mn_3O_4. MnOOH disrupts the CO_2 reduction, introducing defects that can act as charge recombination centers, thereby shortening the charge carrier lifetime. On the other hand, for MT1.1 and MT1.2 samples, the MnOOH phase disappeared, but they contained a large portion of $MnCl_2$ byproduct, which could interfere with surface properties, leading to inefficient charge utilization and poor performance. Therefore, MT1.0 exhibited the highest photocatalytic CO_2 reduction performance because it consists solely of the Mn_3O_4 phase. To further verify the optimal phase of manganese oxide for CO_2 reduction, MnO_2/TiO_2 composite was prepared as a control sample using TTIP instead of $TiCl_4$. As shown in Fig S9, all control samples, including MnO_2/TiO_2, pristine TiO_2 and Mn_3O_4 exhibited lower photocatalytic activity compared to MT1.0. Additionally, GC analysis confirmed that neither H_2 nor CO was produced in detectable quantities. The absence of H_2 indicates that the photogenerated electrons are highly selective toward CO_2 reduction, effectively suppressing the competitive hydrogen evolution reaction [52]. Furthermore, the oxidation reaction was investigated for MT1.0, showing O_2 evolution rate of 9.02 $\mu mol \bullet g^{-1} \bullet h^{-1}$ (Fig. S10). This simultaneous monitoring of reduction and oxidation products confirms the stoichiometric balance [53].

Furthermore, as shown in Fig. 3b, the photocatalytic CO_2 reduction performance did not decrease after four cycles, indicating excellent photostability of MT1.0. However, a decrease in the CH_4 yield was observed in the fifth cycle. This degradation is attributed to the accumulation of reaction intermediates or the poisoning of active sites on the catalyst surface during prolonged exposure to the reaction environment [54]. To further evaluate the durability of the catalyst, post-reaction characterizations were performed. The XRD pattern and TEM images of the MT1.0 catalyst after the reaction showed no significant changes in the crystalline phase or morphology compared to the fresh catalyst (Fig. S11). These results demonstrate that the MT1.0 sample has high durability under the photocatalytic reaction conditions.

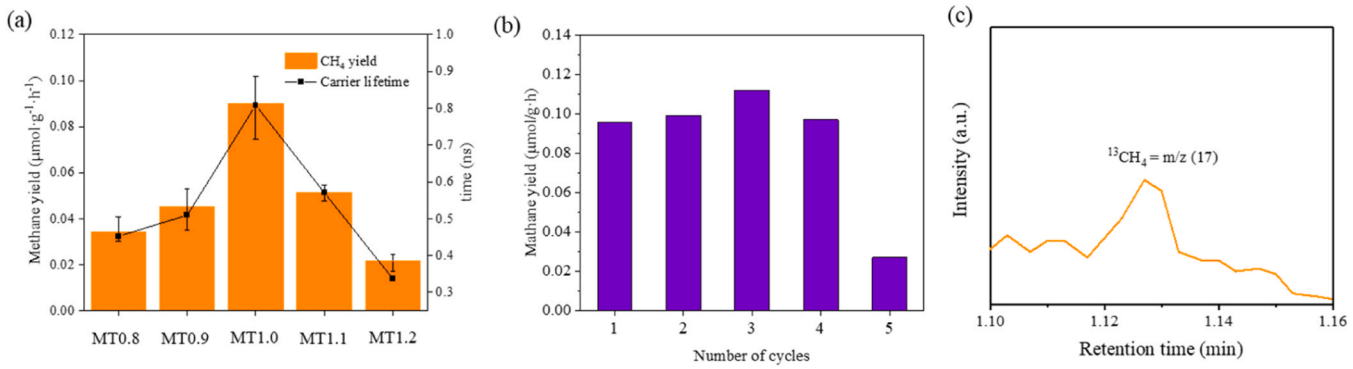


Fig. 3. (a) CH_4 production rate and charge carrier lifetime of MTx samples, (b) the photocatalytic cyclic test by sample MT1.0, and (c) GC-MS spectrum of isotopic $^{13}CH_4$ produced by sample MT1.0 under moist $^{13}CO_2$ atmosphere.

To determine the origin of products, control test and isotope trace test were conducted. The control experiments were carried out with various conditions, *i.e.* without photocatalyst and light, and the presence of He/H_2O instead of CO_2/H_2O. All of control tests show negligible products, confirming that CO_2 is the only carbon source for CH_4 evolution (Fig. S12). A $^{13}CO_2$ isotopic test was performed under the same photocatalytic reaction conditions. The results of GC-MS analysis show that the signal at $m/z = 17$ (Fig. 3c) is matched to $^{13}CH_4$, which is the strong evidence that the produced CH_4 is originated from photocatalytic CO_2 reduction [55]. To further validate the carbon origin of the photocatalytic products, isotopic labeling analysis was performed under 99 % $^{13}CO_2$ atmosphere. As shown in the mass spectrum (Fig. S13), the emergence of a distinct signal at $m/z = 17$ corresponds to the formation of $^{13}CH_4$, confirming that the carbon source of the generated methane is the injected $^{13}CO_2$. The higher intensity of $m/z = 16$ signal compared to $m/z = 17$ is attributed to the $^{13}CH_3^+$ fragment generated during the ionization of the produced $^{13}CH_4$ within the mass spectrum. Additionally, this $m/z = 16$ peak overlaps with background signals from the ^{12}C trace species or residual in the system. Notably, photocatalytic CO_2 conversion performance of MTx sample using diluted CO_2 (1000 ppm) show competitive with previously reported manganese oxide-based materials without the help of photosensitizer or sacrificial agent (Table S4).

3.4. Photocatalytic CO_2 reduction mechanism

To verify the change of the Mn oxidation state during the photocatalytic CO_2 reduction condition, we studied *in situ* Mn K-edge XANES for MT1.0 under reaction conditions.The analysis was conducted under illumination in the presence of CO_2 and H_2O. By comparing the light on/off conditions, it was observed that the oxidation state of Mn ions in the MT1.0 sample is slightly reduced upon illumination (Fig. 4). These results suggest that the photogenerated electrons increased the electron density of the Mn atoms, which can subsequently participate in the photocatalytic CO_2 reduction reaction.

The reaction intermediates for photocatalytic CO_2 reduction process were detected by *in situ* DRIFTS analysis, which are helpful to understand the photocatalytic CO_2 reduction mechanism. Exposing CO_2 and H_2O gas under dark conditions, monodentate carbonate (m-CO_3^{2-}, 1188 cm^{-1}, 1209 cm^{-1}) was detected, which implies CO_2 is adsorbed on the surface of the catalyst (Fig. 5b) [56]. When the light is illuminated to catalyst, new peaks attributed to *CHO (1071, 1053 cm^{-1}), *CH_3O (1067 cm^{-1}), and *COOH (1481 cm^{-1}) were detected, and the intensity of peaks is increased with increasing irradiation time (Fig. 5a). These intermediates have been referred to as crucial intermediates of photocatalytic CO_2 reduction [56]. In contrast, mondentate carbonate peaks decreased according to the increasing illumination time, indicating their conversion into intermediates. Notably, no *CO absorption peak was observed in the range of 2000–2100 cm^{-1}, which implies *CO intermediate rapidly protonated to form *CHO rather than desorbed from the catalyst as CO molecules (Fig. S14). This reaction pathway, which bypasses CO desorption, is responsible for the selective production of CH_4 on MT1.0. It has been well-known that photocatalytic CO_2 reduction reaction were proceeded with proton-assisted electron transfer reaction where H_2O acts as a proton donor [57]. Owing to providing the protons with the consumption of water molecules, the intensity of the OH bending peak at 1630 cm^{-1} was decreased with the extending illumination time (Fig. 5a) [58].

Based on the analysis of reaction intermediates by *in situ* DRIFTS analysis, photocatalytic CO_2 reduction mechanism over MT1.0 can be proposed. Under illumination, photogenerated electrons and protons dissociated from water react with CO_2 molecules adsorbed on the catalyst, which produce *COOH intermediates (Eq. 1). Afterwards, *COOH intermediates react with the photogenerated electrons and protons to form *CO (Eq.2). As *CO rapidly react with electrons and protons to generate *CHO, no *CO intermediates were observed for MT1.0 (Eq. 3). Subsequently, continuous photogenerated electrons and protons react with the intermediates to form *CH_2O, and *CH_3O radicals, (Eqs. 4,5), and finally CH_4 is generated (Eq. 6). H_2O is dissociated to protons and acts as a proton donor to proceed photocatalytic CO_2 reduction (Eq. 7).

$$CO_2 + e^- + H^+ \rightarrow *COOH \quad (1)$$

$$*COOH + e^- + H^+ \rightarrow *CO + H_2O \quad (2)$$

$$*CO + e^- + H^+ \rightarrow *CHO \quad (3)$$

$$*CHO + e^- + H^+ \rightarrow *CH_2O \quad (4)$$

$$*CH_2O + e^- + H^+ \rightarrow *CH_3O \quad (5)$$

$$*CH_3O + 3e^- + 3H^+ \rightarrow CH_4 + H_2O \quad (6)$$

$$H_2O + 2\,h^+ \rightarrow H^+ + OH^* \quad (7)$$

4. Conclusions

In conclusion, we have developed a synthesis method to engineer the phase of manganese oxide for Mn_3O_4/TiO_2 photocatalyst for efficient CO_2 reduction. We identified that the concentration of the $TiCl_4$

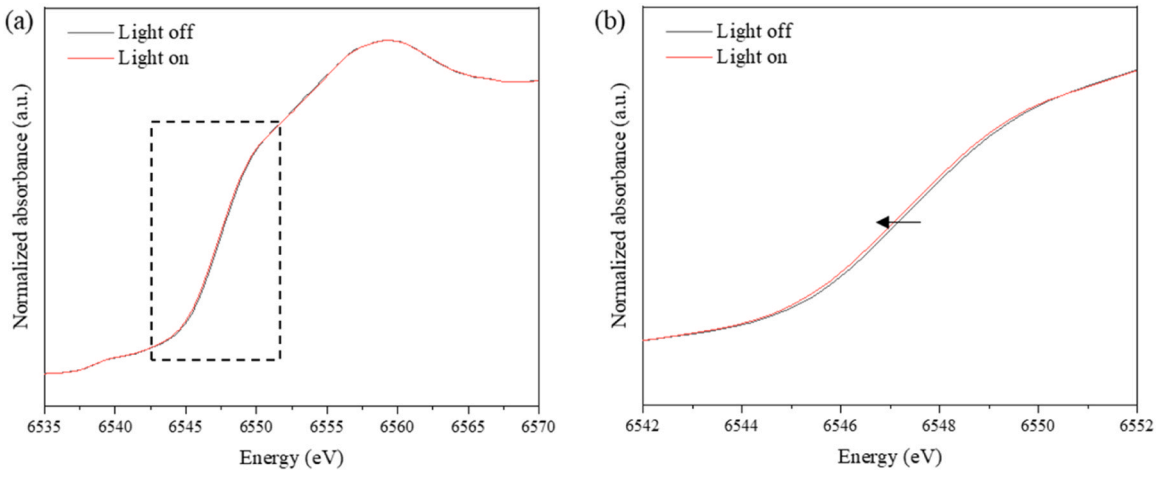


Fig. 4. (a) *In situ* Mn K-edge XANES spectra of MT1.0 sample under the atmosphere of humid CO_2, and (b) the magnified spectra of (a) in the region of 6542–6552 eV.

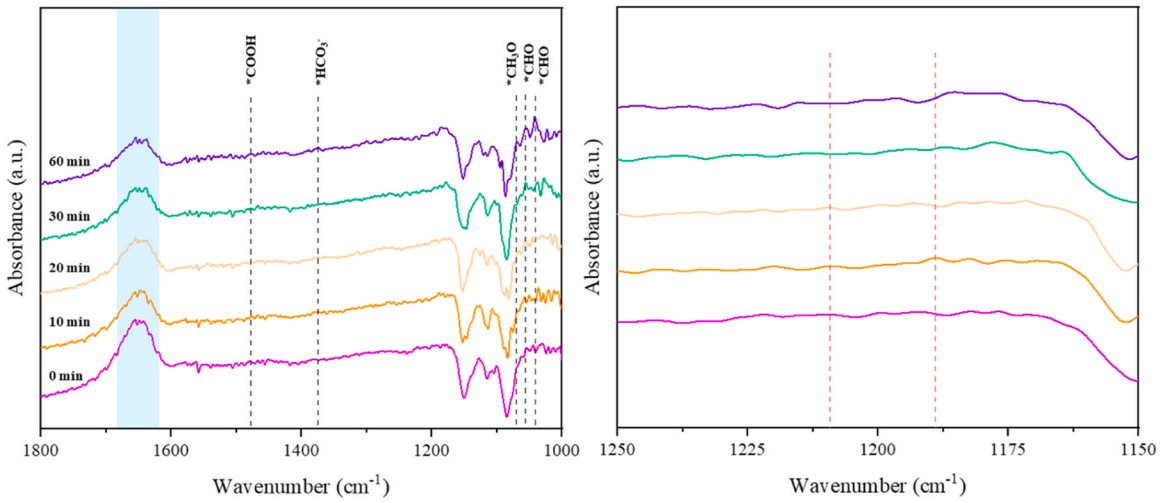


Fig. 5. *In situ* DRIFTS spectra of MT1.0 for photocatalytic CO_2 reduction under illumination: (a) 1000–1800 cm^{-1} and (b) 1150 – 1250 cm^{-1}.

precursor critically determines the final manganese oxide phase. The highest CH_4 evolution rate by Mn_3O_4/TiO_2 catalyst showed 20.1, 7.8 times higher than that of pristine TiO_2 and Mn_3O_4, respectively. Importantly, we found the importance of phase control that when the manganese oxide was less reduced or contained synthetic byproducts, the photocatalytic activity was significantly decreased. The enhanced activity of the optimal MT1.0 catalyst is attributed to broad light absorption, excellent charge separation and longer lifetimes of charge carriers. Furthermore, the lifetime of charge carriers for MTx samples shows a similar trend to the photocatalytic activity of MTx samples. Based on the XPS and *in situ* XANES analysis, this work reveals that the structure-activity relationship between the manganese oxidation state and the photocatalytic performance is highly correlated. This study provides new a synthetic pathway for engineering, the phase of the transition metal oxide catalysts for solar fuels application.

CRediT authorship contribution statement

Eunhee Gong: Writing – review & editing, Writing – original draft, Investigation, Formal analysis, Data curation, Conceptualization. **Yunju Hwang:** Formal analysis, Data curation. **Hye Rim Kim:** Investigation, Formal analysis, Data curation, Conceptualization. **Jin-Woo Jung:** Formal analysis. **Jeonghyeon Lee:** Formal analysis. **In Young Kim:** Writing – review & editing, Data curation. **Chang-Hee Cho:** Validation. **Su-Il In:** Writing – review & editing, Supervision, Project administration, Funding acquisition, Conceptualization.

Declaration of Competing Interest

The authors declare that they have no known competing financial interests or personal relationships that could have appeared to influence the work reported in this paper.

Acknowledgements

S.I.I. acknowledges funding from the National Research Foundation of Korea (NRF) grant (2021R1A2C2009459) and the InnoCORE program of the Ministry of Science and ICT (1.260005.01). I.Y.K was supported by a National Research Foundation of Korea (NRF) grant funded by the Korean government (MSIT) (RS-2024-00350241). X-ray absorption spectra was obtained from Pohang Accelerator Laboratory (PAL) 10 C beamline.

Appendix A. Supporting information

Supplementary data associated with this article can be found in the online version at doi:10.1016/j.jcou.2026.103357.

Data availability

Data will be made available on request.

References

[1] S. Fang, M. Rahaman, J. Bharti, E. Reisner, M. Robert, G.A. Ozin, Y.H. Hu, Photocatalytic CO_2 reduction, Nat. Rev. Methods Prim. 3 (2023) 61–81.
[2] E. Gong, S. Ali, C.B. Hiragond, H.S. Kim, N.S. Powar, D. Kim, H. Kim, S.-I. In, Solar fuels: research and development strategies to accelerate photocatalytic CO_2 conversion into hydrocarbon fuels, Energy Environ. Sci. 15 (2022) 880–937.
[3] J. Lei, H. Yang, B. Weng, Y.-M. Zheng, S. Chen, P.W. Menezes, S. Meng, Optimization of Adsorption Sites for Selective Hydrobenzoin and Syngas Production in a Single Photoredox Cycle, Adv. Energy Mater. 15 (2025) 2500950–2500958.
[4] B.-H. Lee, E. Gong, M. Kim, S. Park, H.R. Kim, J. Lee, E. Jung, C.W. Lee, J. Bok, Y. Jung, Y.S. Kim, K.-S. Lee, S.-P. Cho, J.-W. Jung, C.-H. Cho, S. Lebègue, K.T. Nam, H. Kim, S.-I. In, T. Hyeon, Electronic interaction between transition metal single-atoms and anatase TiO_2 boosts CO_2 photoreduction with H_2O, Energy Environ. Sci. 15 (2022) 601–609.
[5] R. Hua, J. Zhao, H. She, L. Wang, J. Huang, Q. Wang, Valence-state engineering of Cu species on TiO_2 surfaces for synergistic enhancement of photocatalytic CO_2 reduction activity and products selectivity, Chem. Eng. J. 521 (2025) 166444–166454.
[6] C. Wang, T. Xu, K. Gao, L. Jin, C. Guo, W. Wang, Yong Hu, Carbon Doping Synergistically Regulates Carrier Separation Kinetics and Elementary Reaction Thermodynamics for Efficient CO_2 Photoreduction on Zn-Polar ZnO Nanocobbles, Appl. Catal. B Environ. 383 (2026) 126025. -126035.
[7] Y. Han, Z. Jia, W. Gong, X. Wei, Y. Zhang, M. Tao, Y. Ren, Z. Lu, Y. Wu, J. Chen, Z. Shi, Z. Zhao, Z. Zhao, Slow-light-driven photocatalytic CO_2 reduction to CH_4 mediated by photonic crystal Graphdiyne-Cu/ZnO Z-scheme system, Chem. Eng. J. 500 (2024) 157636–157648.
[8] K. Lin, P. Qiao, Q. Liu, Y. He, X. Kang, D. Wang, C. Tian, A. Wu, H. Fu, Hollow TiO_2/CdS Z-Scheme Heterojunctions with Spatially Separated Cocatalysts for Highly Selective Photodriven CO_2 Conversion, Adv. Funct. Mater. (2025) e15276.
[9] H. Su, W. Wang, R. Shi, H. Tang, L. Sun, L. Wang, Q. Liu, T. Zhang, Recent advances in quantum dot catalysts for hydrogen evolution: Synthesis, characterization, and photocatalytic application, Carbon Energy 5 (2023) e280.
[10] J. Lei, N. Zhou, S. Sang, S. Meng, J. Low, Y. Li, Unraveling the roles of atomically-dispersed Au in boosting photocatalytic CO_2 reduction and aryl alcohol oxidation, Chin. J. Catal. 65 (2024) 163–173.
[11] D. Kim, W. Ko, B.-H. Lee, S. Kim, Y.D. Kim, H. Ahn, Y. Jung, C.W. Lee, K.-S. Lee, E. Gong, J. Lee, M. Kim, T. Hyeon, Su-Il In, Atomic Tuning of Metal-Support Interactions for Pathway-Selective CO_2 Photoreduction on TiO_2, Adv. Sci. 0 (2026) e21625.
[12] S. Hejazi, S. Mohajernia, B. Osuagwu, G. Zoppellaro, P. Andryskova, O. Tomanec, S. Kment, R. Zboril, P. Schmuki, On the Controlled Loading of Single Platinum Atoms as a Co-Catalyst on TiO_2 Anatase for Optimized Photocatalytic H_2 Generation, Adv. Mater. 32 (2020) 1908505–1908553.

[13] N.U.M. Nor, E. Mazalan, C. Risko, M. Crocker, N.A.S. Amin, Unveiling the structural, electronic, and optical effects of carbon-doping on multi-layer anatase TiO_2 (1 0 1) and the impact on photocatalysis, Appl. Surf. Sci. 586 (2022) 152641–152653.
[14] J. Wang, H. Zhang, Y. Nian, Y. Chen, H. Cheng, C. Yang, Y. Han, X. Tan, J. Ye, T. Yu, Disruption symmetric crystal structure favoring photocatalytic CO_2 reduction: reduced *COOH formation energy barrier on Al doped CuS/TiO_2, Adv. Func. Mater. 34 (2024) 2406549–2406558.
[15] M. Zoric, P. Basera, L. Palmer, A. Aitbekova, N. Riggs, H. Lim, W. Hu, A. Esparza, H. Sarker, F. Pedersen, H. Atwater, S. Cushing, M. Bajdich, A. Cordones, Oxidizing Role of Cu Cocatalysts in Unassisted Photocatalytic CO_2 Reduction Using p-GaN/Al_2O_3/Au/Cu Heterostructures, ACS Nano 18 (2024) 19538–19548.
[16] S. Sorcar, Y. Hwang, J. Lee, H. Kim, K.M. Grimes, C.A. Grimes, J.-W. Jung, C.-H. Cho, T. Majima, M.R. Hoffmann, S.-I. In, CO_2, water, and sunlight to hydrocarbon fuels: a sustained sunlight to fuel (Joule-to-Joule) photoconversion efficiency of 1%, Energy Environ. Sci. 12 (2019) 2685–2696.
[17] A. Wang, S. Wu, J. Dong, R. Wang, J. Wang, J. Zhang, S. Zhong, S. Bai, Interfacial facet engineering on the Schottky barrier between plasmonic Au and TiO_2 in boosting the photocatalytic CO_2 reduction under ultraviolet and visible light irradiation, Chem. Eng. J. 404 (2021) 127145–127153.
[18] R. Shi, Y. Chen, Controlled Formation of Defective Shell on TiO_2 (001) Facets for Enhanced Photocatalytic CO_2 Reduction, Chemcatchem 11 (2019) 2270–2276.
[19] S. Choi, M.S. Choe, D. Lee, S. Kim, K.-R. Wee, J.Y. Shin, H.-J. Son, Efficient Photosensitization of π-Extended Oligomeric Porphyrin Pigments through TiO2-Mediated Outer-Sphere Electron Transfer in Photochemical CO_2 Reduction Systems, ACS Appl. Energy Mat. 7 (2024) 3602–3617.
[20] Y.-F. Liu, G. Lan, T. Niu, H. Du, M.-D. Dai, J. Sun, Y.-W. Zhang, In-Situ Assembly of Self-Photosensitizing Crystalline Copper(I) Coordination Networks for Photocatalytic CO_2 Reduction, JACS Au 5 (2025) 3045–3051.
[21] J.Y. Wang, H.Y. Zhang, Y. Nian, Y.Q. Chen, H.L. Cheng, C. Yang, Y. Han, X. Tan, J. H. Ye, T. Yu, Disruption symmetric crystal structure favoring photocatalytic CO_2 reduction: reduced *COOH formation energy barrier on Al doped, CuS/TiO_2 34 (2024) 2406549–2406558.
[22] C. Liu, P. Wu, J. Wu, J. Hou, H. Bai, Z. Liu, Effective protect of oxygen vacancies in carbon layer coated black TiO_{2-x}/CNNS hetero-junction photocatalyst, Chem. Eng. J. 359 (2019) 58–68.
[23] G. Lavanya, A. S, B.S. Nishchith, Y. Kalegowda, B.S. Ravikumar, M.H. Braga, Effect of oxidizer-to-fuel ratio on manganese oxides formation and their physico-chemical properties towards supercapacitor application, Chem. Eng. J. 522 (2025) 167669–167681.
[24] J. Yesuraj, S. Vajravijayan, R. Yang, N. Nandhagopal, K. Gunasekaran, N.C. S. Selvam, P.J. Yoo, K. Kim, Self-assembly of hausmannite Mn_3O_4 triangular structures on cocosin protein scaffolds for high energy density symmetric supercapacitor application, Langmuir 38 (2022) 2928–2941.
[25] Y. Jing, A. Fan, J. Guo, T. Shen, S. Yuan, Y. Chu, Synthesis of an ultrathin MnO_2 nanosheet-coated Bi_2WO_6 nanosheet as a heterojunction photocatalyst with enhanced photocatalytic activity, Chem. Eng. J. 429 (2022) 132193–132205.
[26] C. Xia, J. Teng, L. Yue, Y. Zheng, Y. Chu, L. Zhuang, L. Zhao, Y. He, Enhanced photocatalytic nitrogen fixation over MnO_x-modified O-$KNbO_3$: impact of oxygen vacancies and MnOx loading, J. Mater. Chem. C. 13 (2025) 15059–15069.
[27] M.S. Osgouei, M. Khatamian, H. Kakili, Improved visible-light photocatalytic activity of Mn_3O_4-based nanocomposites in removal of methyl orange, Mater. Chem. Phsy 239 (2020) 122108–122118.
[28] J. Luo, L. Steier, M.K. Son, M. Schreier, M.T. Mayer, M. Gratzel, Cu_2O Nanowire Photocathodes for Efficient and Durable Solar Water Splitting, Nano Lett. 16 (2016) 1848–1857.
[29] G. Ghadimkhani, N.R. de Tacconi, W. Chanmanee, C. Janaky, K. Rajeshwar, Efficient solar photoelectrosynthesis of methanol from carbon dioxide using hybrid CuO-Cu_2O semiconductor nanorod arrays, Chem. Commun. 49 (2013) 1297–1299.
[30] K.Q. Lu, J.G. Hao, Y. Wei, B. Weng, S. Ge, K. Yang, S. Lu, M.Q. Yang, Y. Liao, Photocatalytic Conversion of Diluted CO_2 into Tunable Syngas via Modulating Transition Metal Hydroxides, Inorg. Chem. 63 (2024) 795–802.
[31] Z. Liu, K. Xu, H. Sun, S. Yin, One-Step Synthesis of Single-Layer MnO_2 Nanosheets with Multi-Role Sodium Dodecyl Sulfate for High-Performance Pseudocapacitors, Small 11 (2015) 2182–2191.
[32] J. Wu, W. Wang, Y. Tian, C. Song, H. Qiu, H. Xue, Piezotronic effect boosted photocatalytic performance of heterostructured $BaTiO_3$/TiO_2 nanofibers for degradation of organic pollutants, Nano Energy 77 (2020) 105122–105131.
[33] S.Y. Zhu, Y.F. Yuan, P.F. Du, C.L. Mo, G.C. Cai, B.X. Wang, S.Y. Guo, Ultrasmall Mn_3O_4 nanocrystalline@three-dimensional macroporous honeycomb-like hollow carbon matrix for high-rate and long-lifetime zinc-ion storage, Electrochim. Acta 419 (2022) 140396–140404.
[34] M. Aronniemi, J. Sainio, J. Lahtinen, Chemical state quantification of iron and chromium oxides using XPS: the effect of the background subtraction method, Surf. Sci. 578 (2005) 108–123.
[35] S. Zhao, Y. Liu, Y. Wu, H. Zhang, D. Zhang, Y. Zhang, H. Deng, G. Sun, H. Li, W. Shan, H. He, Elucidating atomic structure and reconstruction of Mn_3O_4 (001) surface, Appl. Surf. Sci. 680 (2025) 161339–161356.
[36] N. Li, Y. Tian, J. Zhao, J. Zhang, J. Zhang, W. Zuo, Y. Ding, Efficient removal of chromium from water by Mn_3O_4@ZnO/Mn_3O_4 composite under simulated sunlight irradiation: Synergy of photocatalytic reduction and adsorption, Appl. Catal. B: Environ. Energy 214 (2017) 126–136.
[37] J. Liu, J. Liu, W. Song, F. Wang, Y. Song, The role of electronic interaction in the use of Ag and Mn_3O_4 hybrid nanocrystals covalently coupled with carbon as advanced oxygen reduction electrocatalysts, J. Mater. Chem. A 2 (2014) 17477–17488.
[38] F. Xu, J. Zhang, B. Zhu, J. Yu, J. Xu, $CuInS_2$ sensitized TiO_2 hybrid nanofibers for improved photocatalytic CO_2 reduction, Appl. Catal. B: Envrion.Energy 230 (2018) 194–202.
[39] Y. Zhang, N. Cao, H. Cheng, X. Zhao, L. Qiu, Y. Fang, J. Liao, X. Cai, X. Tian, L. Lei, P. Xie, X. Zhang, Interface reconfiguration of $MnCO_3$/Mn_3O_4 heterostructure enhances the ozone decomposition in the entire humidity range, Appl. Catal. B: Environ. Energy 355 (2024) 124171–124180.
[40] B.W. Dai, B. Zhang, J. Ji, B. Liu, R. Xie, Y. Gan, X. Xie, J. Zhang, P. Huang, H. Huang, Exceptional ozone decomposition over δ-MnO_2/AC under an entire humidity environment, Environ. Sci. Technol. 57 (2023) 17727–17736.
[41] K.P. Murugan, S. Sabarinathan, N. Prabhakaran, S. Swarnalatha, Valorization of hazardous chrome tanned leather buffing waste for the production of Cr_2O_3/carbon/TiO_2 composite semiconductors with the removal of chlorophenol from its wastewater, Chem. Eng. J. 468 (2023) 143547–143561.
[42] C. Cheng, W.H. Fang, R. Long, O.V. Prezhdo, Water Splitting with a Single-Atom Cu/TiO_2 Photocatalyst: Atomistic Origin of High Efficiency and Proposed Enhancement by Spin Selection, JACS Au 1 (2021) 550–559.
[43] J. Tauc, R. Grigorovici, A. Vancu, Optical Properties and Electronic Structure of Amorphous Germanium, Phys. Stat. Sol. 15 (1966) 627–637.
[44] Y. Ma, J. Jiang, A. Zhu, P. Tan, Y. Bian, W. Zeng, H. Cui, J. Pan, Enhanced visible-light photocatalytic degradation by Mn_3O_4/CeO_2 heterojunction: a Z-scheme system photocatalyst, Inorg. Chem. Front 5 (2018) 2579–2586.
[45] M.G. Kim, J.M. Kang, J.E. Lee, K.S. Kim, K.H. Kim, M. Cho, S.G. Lee, Effects of Calcination Temperature on the Phase Composition, Photocatalytic Degradation, and Virucidal Activities of TiO_2 Nanoparticles, ACS Omega 6 (2021) 10668–10678.
[46] Z. Zou, Y. Wang, T. Zhang, J. Lu, V. Turkevich, Y. Yu, J. Xu, H. Lin, Y. Li, L. Wang, Hollow p-n heterostructures with vacancy engineering to enhance Z-scheme photocatalytic CO_2 reduction, Chem. Eng. J. 520 (2025) 165595–165607.
[47] S. Ma, M.E. Reish, Z. Zhang, I. Harrison, J.T. Yates, Anatase-Selective Photoluminescence Spectroscopy of P25 TiO_2 Nanoparticles: Different Effects of Oxygen Adsorption on the Band Bending of Anatase, J. Phys. Chem. C. 121 (2017) 1263–1271.
[48] A. Sabbah, I. Shown, M. Qorbani, F.Y. Fu, T.Y. Lin, H.L. Wu, P.W. Chung, C. Wu, S. R.M. Santiago, J.L. Shen, K.H. Chen, L.C. Chen, Boosting photocatalytic CO_2 reduction in a ZnS/$ZnIn_2S_4$ heterostructure through strain-induced direct Z-scheme and a mechanistic study of molecular CO_2 interaction thereon, Nano Energy 93 (2022) 106809–106821.
[49] A. Mimura, M. Fujii, S. Hayashi, K. Yamamoto, Quenching of photoluminescence from Si nanocrystals caused by boron doping, Solid State Commun. 109 (1999) 561–565.
[50] S. Hu, P. Qiao, X. Liang, G. Ba, X. Zu, H. Hu, J. Ye, D. Wang, Single-atom Pt–N_4 active sites anchored on porous C_3N_4 nanosheet for boosting the photocatalytic CO_2 reduction with nearly 100% CO selectivity, Appl. Catal. B: Environ. Energy 346 (2024) 123737–123745.
[51] K. Takanabe, Photocatalytic Water Splitting: Quantitative Approaches toward Photocatalyst by Design, ACS Catal. 7 (2017) 8006–8022.
[52] S. Cheng, Z. Sun, K.H. Lim, T.Z.H. Gani, T. Zhang, Y. Wang, H. Yin, K. Liu, H. Guo, T. Du, L. Liu, G.K. Li, Z. Yin, S. Kawi, Emerging Strategies for CO_2 Photoreduction to CH_4: From Experimental to Data-Driven Design, Adv. Energy Mat. 12 (2022) 22000389–22200426.
[53] H. Shi, Z. Li, S. Chen, Y. Yao, L. Wu, R. Shao, C. Sheng, S. Zhong, D. Wang, Y. Zhao, L. Zhao, S. Bai, Facet engineering of MOF supports regulates product selectivity in CO_2 photoreduction by modulating electron and proton supply to COF shells, Chem. Sci. 16 (2025) 17688–17702.
[54] C.B. Hiragond, S. Biswas, N.S. Powar, J. Lee, E. Gong, H. Kim, H.S. Kim, J.-W. Jung, C.-H. Cho, B.M. Wong, S.-I. In, Carbon Energy 6 (2024) e386.
[55] C.B. Hiragond, J. Lee, H. Kim, J.-W. Jung, C.-H. Cho, S.-I. In, A novel N-doped graphene oxide enfolded reduced titania for highly stable and selective gas-phase photocatalytic CO_2 reduction into CH_4: An in-depth study on the interfacial charge transfer mechanism, Chem. Eng. J. 416 (2021) 127978–127989.
[56] K. Lai, Y. Sun, N. Li, Y. Gao, H. Li, L. Ge, T. Ma, Photocatalytic CO_2-to-CH_4 Conversion with Ultrahigh Selectivity of 95.93% on S-Vacancy Modulated Spatial In_2S_3/In_2O_3 Heterojunction, Adv. Funct. Mater. 34 (2024) 2409031–2409042.
[57] C.B. Hiragond, N.S. Powar, J. Lee, S.I. In, Single-Atom Catalysts (SACs) for Photocatalytic CO_2 Reduction with H_2O: Activity, Product Selectivity, Stability, and Surface Chemistry, Small 18 (2022) 2201428–2201465.
[58] P. Liu, Z. Huang, X. Gao, X. Hong, J. Zhu, G. Wang, Y. Wu, J. Zeng, X. Zheng, Synergy between Palladium Single Atoms and Nanoparticles via Hydrogen Spillover for Enhancing CO_2 Photoreduction to CH_4, Adv. Mat. 34 (2022) 2200057–2200067.